International Journal of Applied Earth Observations and Geoinformation 95 (2021) 102255

Contents lists available at ScienceDirect

International Journal of Applied Earth Observations and Geoinformation

journal homepage: www.elsevier.com/locate/jag

An updated MODIS global urban extent product (MGUP) from 2001 to 2018 based on an automated mapping approach

Xin Huang [a,b], Jiongyi Huang [a], Dawei Wen [c,*], Jiayi Li [a,*]

[a] School of Remote Sensing and Information Engineering, Wuhan University, Wuhan 430079, China
[b] State Key Laboratory of Information Engineering in Surveying, Mapping and Remote Sensing, Wuhan University, Wuhan 430079, China
[c] College of Public Administration, Huazhong Agricultural University, Wuhan 430070, China

ARTICLE INFO

Keywords:
Global urban land
Samples
Classification
MODIS
Global mapping

ABSTRACT

Timely and accurate global urban maps are fundamental in monitoring urbanization process and understanding environmental degradation. Therefore, this paper proposed a locally adaptive and fully automated global mapping method and produced an updated 250 m MODIS global urban area product (MGUP) from 2001 to 2018. The proposed approach mainly consists of 1) automated samples extraction from existing global products, 2) locally adaptive samples selection and trained classification in each 5° × 5° grid, and 3) post-processing in terms of the spatio-temporal context. To validate the product, 9 groups of samples for every two years from 2001 to 2018, amounting to over 150,000 sample points, were collected manually from Landsat imagery as global validation dataset. Accuracy assessment indicates that MGUP has a F-score of 0.88, achieving better results than the contemporary global products, i.e., MCD12Q1.v5 (0.82), MCD12Q1.v6 (0.86), and CCI-LC (0.86). Analysis of urban expansion based on MGUP shows that the world's urban area increased to 802233 km^2 and accounted for 0.54% of the Earth's land surface in 2018. The total global urban area expanded by 1.68 times from 2001 to 2018. At continent level, urban density varies considerably, and the highest and lowest one is in Europe (1.78%) and Oceania (0.15%), respectively. At national level, large increment of urban area mainly occurs in North America, Asia, and South America; and countries having high growth rates are mainly developing countries in Africa and Asia. MGUP can be downloaded at https://www.researchgate.net/publication/339873537_MGUP_annual_global_2001_2018.

1. Introduction

Rapid urbanization is sweeping the globe, as indicated by the compelling evidence that the proportion of urban population from 1960′s 33% to today's 55% (UN, 2018). Dense population and various social-economic activities concentrating in urban areas cause profound impacts on biodiversity (McDonald et al., 2013; Pauchard et al., 2006), hydrology (Carlson and Arthur, 2000; Shao et al., 2019), air pollution (Han et al., 2014; Li et al., 2012), health (Moore et al., 2003; Nicolaou et al., 2005), and resource consumption (Madlener and Sunak, 2011; Poumanyvong and Kaneko, 2010), yet relation of urbanization and environment remains controversial and still arouses public concerns (Seto et al., 2010). Therefore, timely and accurate depiction of urban area is of vital importance to monitor urbanization process, which provides essential data for environmental research (Wang et al., 2012).

Urban extent mapping at global scale offers a macro scenario to explore imbalance of urbanization development among regions. The contemporary global urban maps are summarized in Table 1, which can be divided into three types according to their spatial resolution: the coarse (≥1 km), moderate (250–500 m), and high (≥30 m) resolution products. Coarse-resolution products are difficult in depicting small-size urban areas and solving the mixed pixel problem (Schneider et al., 2010; Yang et al., 2017). More importantly, the increased spatial resolution of global urban maps allows detailed delineation of urban area. Whereas, global mapping with high-resolution imagery is subject to heavy computational burden due to the large data volume to be processed. Thanks to the development of data storage and process capability, it is becoming feasible to delineate urban areas at finer resolution. However, relatively high-resolution sensors, such as Landsat, is difficult in providing consistent global coverage of data at annual or higher observation frequency. Therefore, considering the huge computation cost and unavailability of high-resolution data, medium-resolution

* Corresponding authors.
E-mail addresses: daweiwen@mail.hzau.edu.cn (D. Wen), zjjerica@whu.edu.cn (J. Li).

https://doi.org/10.1016/j.jag.2020.102255
Received 12 July 2020; Received in revised form 5 October 2020; Accepted 20 October 2020
Available online 5 November 2020

Table 1
The global urban products presented in order of increased spatial resolution.

Products	Time	Resolution	Definition of urban	References
Global Land Cover-SHARE (GLC-SHARE)	2012	1000 *m*	Artificial surfaces	(Latham et al., 2014)
Global Land Cover 2000 (GLC2000)	2000	998 *m*	Artificial surfaces and associated areas	(Bartholome and Belward, 2005)
Global Rural-Urban Mapping Project (GRUMP)	1995	927 *m*	Urban extent	(CIESIN, 2004)
The MODIS Land Cover Type product (MCD12Q1)	2001–2013/ 2001–2018	500 *m*	Urban and built-up areas	(Friedl et al., 2010; Sulla-Menashe et al., 2019)
GlobCover	2004–2006, 2009	300 *m*	Artificial surfaces and associated areas	(Bontemps et al., 2011; Defourny et al., 2006)
ESA Climate Change Initiative land cover maps (CCI-LC)	1992–2015	300 *m*	Urban extent	(ESA, 2017)
Global land cover types at 250 m resolution (GLC250 m_CN)	2001, 2010	250 *m*	Impervious surfaces	(Wang et al., 2015)
Finer Resolution Observation and Monitoring of Global Land Cover (FROM-GLC)	2010	30 *m*	Impervious surfaces	(Gong et al., 2013)
China's 30 m GLC data product (GlobeLand30)	2000, 2010	30 *m*	Artificial surfaces	(Chen et al., 2015)
Global Urban Land	1990–2010	30 *m*	Impervious surfaces	(Liu et al., 2018)
Global Artificial Impervious Area (GAIA)	1985–2018	30 *m*	Artificial impervious surfaces	(Gong et al., 2020)

remote sensing imagery is still an appropriate data source for developing continuous global urban extent products.

Among moderate-resolution sensors, MODIS (Moderate Resolution Imaging Spectrometer) is regarded as an ideal data source for global mapping considering its high temporal resolution (nearly daily visit of the globe) and free accessibility (Boschetti et al., 2015; Estel et al., 2015). More frequent cloud-free observations allow it to capture detailed temporal signature of phenological information, which is beneficial for distinguishing urban from other land covers (Schneider et al., 2010). A number of efforts have been made to delineate global urban area with MODIS data (Huang et al., 2016; Mertes et al., 2015; Schneider et al., 2010), of which the MODIS Land Cover Type product (MCD12Q1) is the most widely used one with continuous and long time series. The user's accuracy of urban area for MCD12Q1 products is over 90% through cross-validation analysis since no independent validation data set at global scale is available (Schneider et al., 2010; Sulla-Menashe et al., 2019). Some studies reported the overestimation of this product along the city boundaries (Wan et al., 2015). Hence, making full use of the high-temporal advantages of MODIS data to produce more reliable and continuous global urban maps still needs to be explored.

Among a number of global mapping methods, supervised classification is widely adopted due to superiority in strong adaptability and fine mapping accuracy (Friedl et al., 2010; Gong et al., 2013; Schneider et al., 2010; Sulla-Menashe et al., 2019). It is well agreed that the quality of training samples, e.g., size, distribution, and representativeness, strongly affect performance of supervised methods (Pal and Mather, 2006), even more than the impact of classifier (Li et al., 2014). However, using conventional ground survey or visual interpretation, collection of high-quality samples at the global scale is labor and cost intensive, not to mention over a long-term basis for continuous mapping (Radoux et al., 2014; Yifang et al., 2015). However, it should be noted that the land cover information in the existing maps is potential for collection of time-series samples.

Within this context, we adopted the definition of urban areas in the MCD12Q1 products, i.e., more than 30% impervious surface area. This research presents an annual 250 m global urban area product from 2001 to 2018 by proposing an automated mapping approach. The proposed method includes the following three steps:

1) Automated sample extraction based on urban probability from the existing products and spatio-temporal constraints to reinforce the diversity and representativeness of samples;

2) Locally adaptive sample selection and classification method in each $5^\circ \times 5^\circ$ grid to mitigate the interference from regional differences in urban morphology;

3) Post-processing in a spatio-temporal context to improve classification reliability and temporal consistency.

To validate our product (namely, MGUP, updated global urban product), 9 groups of samples for every two years from 2001 to 2018, amounting to over 150,000 spatially independent sample points, were collected as global validation dataset. The results were compared against the reference data and other contemporary global urban products. Finally, analysis of urban land expansion at global, continent, and national scale was conducted using our annual MGUP.

2. Methods

The proposed approach is composed of five blocks: 1) establishment of training sample pools, 2) locally adaptive sample selection based on Kullback-Leibler divergence, 3) features and classifiers, 4) post-processing in a spatio-temporal context, and 5) accuracy assessment.

2.1. Establishment of training sample pools

Extraction of highly reliable global samples in an appropriate manner is the key to developing global mapping methods. The existing maps, containing a wealth of urban information, are actually potential for providing automated training samples at global level. However, there are two problems while extracting information from the existing urban maps. One is the incompatible urban definition in different products and the other is the errors in these maps (Radoux et al., 2014). To deal with the aforementioned issues, we proposed an automated sample extraction method involving 1) urban probability from the existing urban extent products and 2) spatio-temporal constraints to reinforce the diversity and representativeness of the samples.

Specifically, four state-of-the-art medium-resolution urban products, GlobCover (Bontemps et al., 2011; Defourny et al., 2006), CCI-LC (ESA, 2017), MCD12Q1.v5 (Friedl et al., 2010), and MCD12Q1.v6 (Sulla-Menashe et al., 2019) (see Table 1), were considered in our research for their similarity in the resolution and definition. These four products are hereafter called urban and built-up (URB) datasets. It should be noted that only URB datasets during 2001–2013 were used here since after 2013 some of them are not available. Therefore, we used the training sample in 2013 for urban mapping after 2013. The establishment of training sample pools is described in detail as follows.

2.1.1. Extraction of urban samples

The workflow of the automated extraction of urban samples for time-series global urban land mapping is presented in Fig. 1, which includes two major steps: (1) identification of potential urban sample location and (2) spatio-temporal constraints.

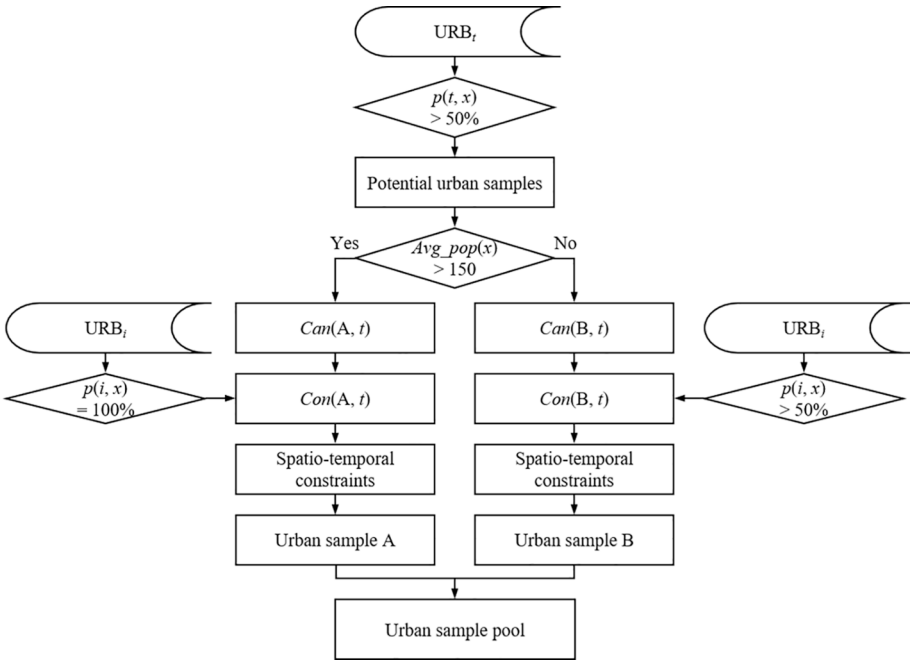

Fig. 1. Workflow of the automated extraction of urban samples for time-series global urban land mapping.

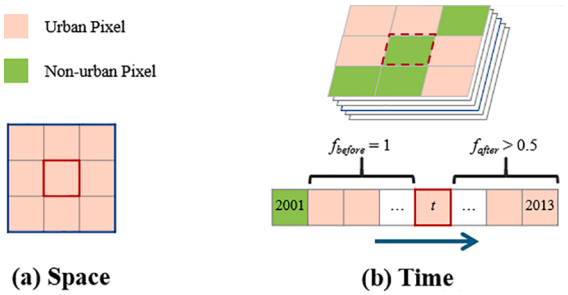

Fig. 2. Graphical diagram of the spatio-temporal constraints.

In step 1, urban probability at pixel × for a certain year t ($p(t, x)$, $t \in i$, i = 2001, 2002, …, 2013) was thresholded with 50% to identify the potential urban sample location x. $p(t, x)$ is defined as the ratio between the times that a pixel is labeled as urban land and the total number of URB datasets available in year t.

In step 2, the potential sample locations were further separated into two groups in terms of high and low population density (i.e., *Can*(A, t) and *Can*(B, t)) using a threshold value of 150 persons per km^2. Here, the average population density in urban patches for pixel × (i.e., *Avg_pop*(x)) was calculated based on the 2015 Global Human Settlement Population Layer (GHS-POP). Urban patches are defined as spatially continuous pixels that have ever been labeled as urban in any URB dataset during 2001 ~ 2013. Different spatio-temporal constraints were applied to these two groups separately, due to the following reasons: (1) In high population density areas, urban samples are abundant and hence, can be extracted more easily; (2) On the other hand, in low density areas, urban samples show different characteristics (e.g., sparse urban areas mixed with natural land covers), which are relatively difficult to be captured from the existing products.

We first constructed two constraint datasets, *Con*(A, t) and *Con*(B, t), respectively, to carry out different spatio-temporal constraints for *Can*(A, t) and *Can*(B, t) for the year t. They were obtained in terms of $p(i, x)$:

$$\begin{aligned} &Con(\mathrm{A}, t) : p(i, x) = 100\%, \\ &Con(\mathrm{B}, t) : p(i, x) > 50\% \\ &with i = 2001, 2002, \cdots, 2013, i \neq t \end{aligned} \quad (1)$$

where $p(i, x)$ denotes the ratio between the times that a pixel is labeled as urban land and the total number of URB datasets available in year i except for t.

Based on the datasets *Con*(A, t) and *Con*(B, t), the proposed spatio-temporal constraints were imposed on *Can*(A, t) and *Can*(B, t), respectively (also demonstrated in Fig. 2):

- *Spatial constraint*:

8 neighboring pixels around urban pixel (x, y) in year t are all urban land;

- *Temporal constraint*:

$f_{before} = 1$and f_{after} greater than 0.5, where f_{before} and f_{after} denote the frequencies of urban land for location (x, y) during the period before and after the year t, respectively.

The sample location × was retained when either condition is satisfied. As aforementioned, urban areas with high and low population density were processed separately, with strong and weak constraints, respectively, since they correspond to dense and sparse urban samples. In this way, more samples can be obtained in the sparse or small urban areas.

After filtering the *Can*(A, t) and *Can*(B, t), the derived sample location A and B were combined as the urban sample pool for year t. When urban sample pool for every year from 2001 to 2013 were established, the sample points that appear in both years $t - 1$ and $t + 1$ were added to the pool of year t, in order to ensure sufficient number of samples.

2.1.2. Extraction of non-urban samples

For extraction of non-urban samples, an erosion filter was used since non-urban areas are large and widely distributed. Firstly, when class labels for pixel × in year t in all the URB datasets are all non-urban area, pixel × was identified as potential non-urban sample. Afterward, a morphological erosion with a radius of 2 km was performed to obtain the final samples. Including both urban and non-urban samples, the sample pool for year t can be established.

Table 2
Input data sources used to produce the MGUP product.

Type	Dataset	Description	Source	Application
Classification	MOD09Q1	Surface Reflectance 8-Day L3 Global 250 *m*	https://ladsweb.modaps.eosdis.nasa.gov	Obtain surface reflectance B1 and B2 for spectral feature extraction.
	MOD09A1	Surface Reflectance 8-Day L3 Global 500 *m*		Obtain surface reflectance B3, B4, B5, B6 and B7 for spectral feature extraction.
	MOD11A2	Land Surface Temperature/ Emissivity 8-Day L3 Global 1 km		Obtain night-time LST for temperature feature extraction.
Auxiliary	GHS-POP	2015 Global Human Settlement Population Layer 1 km	https://ghsl.jrc.ec.europa.eu	Provide population data to assist the establishment of training sample pool.

2.2. Locally adaptive sample selection based on Kullback-Leibler divergence

Some studies indicated that a larger number of training samples can lead to saturation in classification accuracy and decrease in classification efficiency (Heydari and Mountrakis, 2018). Therefore, a locally adaptive sample selection method was proposed in this research to find the best sampling rate in each local region and establish a tradeoff between accuracy and efficiency. Specifically, the global land was divided into grids with the size of $5^\circ \times 5^\circ$. In each grid, the difference between the samples extracted with different rates and all the training data in the sample pool were measured through Kullback-Leibler divergence. The Kullback-Leibler divergence is able to quantify the difference between two probability distributions (Kullback and Leibler, 1951), and a lower value indicates more similarity between them:

$$D_{KL} = \sum_{k=1}^{N} p(f_k) \ln \frac{p(f_k)}{q(f_k)} \tag{2}$$

where D_{KL} is the Kullback-Leibler divergence, N ($N = 1000$) is the number of bins of the histogram for the features of urban sample in a grid, $p(f_k)$ and $q(f_k)$ is the frequency of the feature value f_k in the k^{th} bin for the extracted samples and the entire sample pool in the grid, respectively. The feature values were derived from the first principal component of the features considered in the mapping (see Section 2.3), after the processing of normalization and discretization. Theoretically, as the sampling rate increases, Kullback-Leibler divergence becomes smaller, since the difference between the selected samples and all the training samples in the pool decreases.

To find a proper sampling rate, Kullback-Leibler divergences for different sampling rates from 5% to 50% with an interval of 1% were calculated, and the sampling was repeated 10 times for each sampling rate. Subsequently, a nonlinear function in Eq. (3) was computed for each grid to desribe the relationship between divergence and sampling rate:

$$\overline{D_{KL}} = aR^b + c \tag{3}$$

where R is sampling rate, $\overline{D_{KL}}$ is the fitted Kullback-Leibler divergence, and a, b, and c are fitting coefficients. It is a monotone decreasing and convex function. With this function, when the sampling rate is increased and the divergence does not significantly change, this sampling rate is determined as the optimal one. Therefore, the point where the first derivative of $\overline{D_{KL}}$ equals to -1 was found, and the corresponding sampling rate was adopted for sampling in the grid. For a grid with small number of urban samples, the samples in the neighboring 8 girds were added to the current pool.

2.3. Features and classifiers

The input data sources for classification are shown in Table 2. All the input data were set to WGS 84 and resampled to 250 m for further feature extraction. Our classification approach employed the time series data within each year to fully take advantage of high temporal resolution of MODIS data since vegetation phenology information can improve the discrimination between urban areas and other land cover types (Sung and Li, 2012). Specifically, the four seasons are defined as Winter (Decemeber-Febrary), Spring (Marach-May), Summer (June-August), and Autumn (September-November). In this way, the seasonal spectral and temperature features were extracted since they are potential in discriminating urban areas (Keramitsoglou et al., 2011; Schneider et al., 2010). Spectral features include seasonal composite spectral bands and normalized difference spectral indices. For seasonal composite spectral bands, the 40th quantile of spectral values of data in each season was obtained, which can guarantee data integrity and reduce cloud-coverage influence. Normalized difference spectral indices were adopted since they can maximize the differences between different land cover types (Li et al., 2019). The calculations of these spectral indices are specified below:

$$NDXI = \frac{Band_{(s,u)} - Band_{(s,v)}}{Band_{(s,u)} + Band_{(s,v)}} \tag{4}$$

where *NDXI* denotes normalized difference spectral index; *Band*(*s*,*u*) and *Band*(*s*,*v*) are seasonal composite spectral features in season *s* for channel *u* and *v*, respectively. For seasonal temperature features, mean values of nightime land surface temperature (LST) in each season were adopted. In total, 116 features were fed to the classifier for each year, including 7 composite spectral bands, 21 normalized difference spectral indices, and 1 night-time LST band for each season.

Since random forests classifier has good generalization ability and can handle high dimensional data at relatively low computational cost (Gislason et al., 2006), it was adopted for global urban area mapping from 2001 to 2018 in this study. In addition, to improve the classification efficiency, classification was conducted only for pixels within an urban mask. The urban mask was created by the union of urban pixels in the URB datasets during 2001 ~ 2018, and a 5 km buffer zone was included in the mask to cover all the potential urban areas. Using a locally selected training samples and seasonal features, the random forest classification was performed for pixels in each grid. In this study, the number of random forest tree is set as 10.

2.4. Post-processing in a spatio-temporal context

When the initial classification results were obtained, a post-processing approach was proposed under the assumption of irreversible nature of urbanization process, to deal with the issue of temporal inconsistency (Schneider and Mertes, 2014). The existing algorithms, such as spatio-temporal Markovian classifier (Wehmann and Liu, 2015), bidirectional Markov random field model (Chen et al., 2019) and spatio-temporal transition probability matrix (Liu et al., 2019), have been proved to be effective by considering the spatio-temporal context. However, the high computational cost hinders the implementation of these methods at a global scale. In addition, since there are misclassification errors in the time-series mapping results, the initial classification results should be modified to reduce error progation and improve temporal consistency. In this study, therefore, a new post-processing scheme, including weighted-fusion for correcting the initial results and spatio-temporal filtering, was proposed.

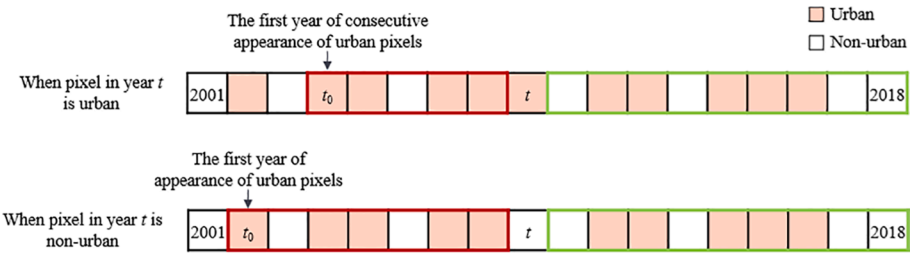

Fig. 3. Schematic diagram on determination of starting year t_0 of the period before year *t*.

2.4.1. Weighted fusion for correcting the initial results

A weighted fusion strategy was designed to reduce classification errors by combing time-series URB datasets and the initial mapping results. The fusion weight values were defined in terms of the classification reliability in different years. The classification reliability was measured as the difference between the average urban area in the URB dataset (*Ref_area*(*g, i*)) and the urban area of our initial classificatin result (*Area*(*g, i*)) in gird *g* of year *i*:

$$Dif_{(g,i)} = \left| Area_{(g,i)} - Ref\_area_{(g,i)} \right| \tag{5}$$

A smaller $Dif_{(g,i)}$ value indicates higher classification reliability. Subsequently, the weight values ($w_1(g, i)$) were assigned for grid *g* in different years on the basis of descending order of $Dif_{(g,i)}$. For instance, the weight values were set to 18 and 1 for years with smallest and largest $Dif_{(g,i)}$ values, respectively.

Subsequently, weighted frequencies of urban area in pixel × during the period before and after year *t*, $f_{fore}(x, t)$ and $f_{back}(x, t)$,were obtained by:

$$f_{fore}(x,t) = \frac{\sum_{i=t_0}^{t-1} w_1(g,i)c(x,i)}{\sum_{i=t_0}^{t-1} w_1(g,i)} \tag{6}$$

$$f_{back}(x,t) = \frac{\sum_{i=t+1}^{2018} w_1(g,i)c(x,i)}{\sum_{i=t+1}^{2018} w_1(g,i)} \tag{7}$$

where $c(x, i)$ is class label for pixel *x* in year *i* with values 0 and 1 representing non-urban and urban area, respectively; t_0 is the starting year of the period before year *t*. As shown in Fig. 3, there are two situations for determination of t_0:

1) When pixel *x* is labeled as urban in year *t*, t_0 is the first year of the consecutive appearance of urban pixels;

2) When pixel *x* is labeled as non-urban in year *t*, t_0 is the first year of appearance of urban pixels.

Using the weighted frequencies $f_{fore}(x, t)$ and $f_{back}(x, t)$, the initial calss label $c(x, t)$ can be modified as $c'(x, t)$ according to the rule described below:

$$c'(x,t) = \begin{cases} 1, c(x,t) = 1 and f_{fore}(x,t) \geq th_1 and f_{back}(x,t) \geq th_1 \\ 1, c(x,t) = 0 and f_{fore}(x,t) \geq 0.98 \\ 0, otherwise \end{cases} \tag{8}$$

$$th_1 = \begin{cases} 0.8, Area(g,t) > Ref\_area(g,t) \\ 0.6, Area(g,t) \leq Ref\_area(g,t) \end{cases} \tag{9}$$

where th_1 is an empirical threshold value.

2.4.2. Spatio-temporal filtering

Only temporal content was considered in the weighted fusion correction, thus, we developed a spatio-temporal filtering to further refine the classification results. Firstly, for each pixel (y_c, z_c) in the time sequence t_c, we calculated its urban probability ($p(y_c, z_c, t_c)$) through the inverse distance weighted average of pixels in a 3 × 3 × 5 spatio-temporal window (a 3 × 3 window in 5 years):

Table 3
Division of city levels based on population.

City levels	Population(thousand)
First level	≥10,000
Second level	1,000 ~ 10,000
Third level	< 1,000

$$p_{(y_c,z_c,t_c)} = \sum_{y=y_c-1}^{y_c+1} \sum_{z=z_c-1}^{z_c+1} \sum_{t=t_c-2}^{t_c+2} w_2(y,z,t) c\_new(y,z,t) \tag{10}$$

where (y_c, z_c, t_c) is the center pixel in the 3 × 3 × 5 spatio-temporal window, and $w_2(y, z, t)$ denotes the weight of pixel (*y*, *z*, *t*). $w_2(y, z, t)$ is calculated based on the normalized inverse distance, and the pixels with larger distance values are assigned as lower weights. Considering the importance of the label of the center pixel (y_c, z_c, t_c), its weight, $w_2(y_c, z_c, t_c)$, is empirically set to 0.1. In this way, a higher value of $p(y_c, z_c, t_c)$ indicates larger confidence that the center pixel is identified as urban. If $p(y_c, z_c, t_c)$ is larger than 50%, the center pixel is labeled as urban, otherwise non-urban. In this way, the initial classfication result can be further improved in a spatio-temporal context. Based on the modified classification result, the final label for each pixel was given according to the assumption of irreversible nature of urbanization process.

2.5. Accuracy assessment

To objectively evaluate our results, global validation samples for every two years from 2001 to 2018, i.e., 9 groups of time-series samples, were collected manually. Using the random-stratified sampling strategy in terms of the population size, 5 cities were randomly selected from the first, second, and third level cities (Table 3), respectively, in each group, generating 135 validation cities. The distribution and details of these cities are presented in Fig. 4 and Table 4, respectively. Over 150,000 sample points were randomly generated and labeled through visual interpretation of Landsat images. In order to ensure the spatial independence among the validation samples, the minimum distance between them is set as 1 km.

Using the validation sample set, we performed accuracy assessment to the proposed MGUP and the current state-of-the-art products including MCD12Q1.v5, MCD12Q1.v6, and CCI-LC, using the F-score measure.

$$Precision = \frac{TP}{TP + FP} \tag{11}$$

$$Recall = \frac{TP}{TP + FN} \tag{12}$$

$$F - score = 2 \times \frac{Precision \times Recall}{Precision + Recall} \tag{13}$$

where *TP* is the number of correctly detected urban pixels, *FP* is the number of non-urban pixels that are wrongly detected as urban, *FN* is the number of urban pixels that are wrongly detected as non-urban, and

Fig. 4. The distribution of validation cities in this research.

Precision and *Recall* indicate correctness and completeness, respectively.

3. Results and discussions

3.1. Visual inspection

The MGUP products were evaluated at global, regional, and city scales. Firstly, the global urban change intensity map at a grid scale of 1° is shown in Fig. 5 to demonstrate the hotspots of urban expansion. The change intensity is the ratio of the size of urban change during 2001 ~ 2018 to the size of the total land area in this grid. It can be observed that the global urban expansion is unevenly distributed, and urban expansion hotspots are mainly located in North America, Europe, and Asia. 4 representative hotspot regions, including Eastern China, United States, Western Europe, and India, are presented in Fig. 6. As indicated by Fig. 6 (d), there is significantly rapid urbanization in Eastern China. In addition, mapping results in the 4 Chinese cities, i.e., Shanghai, Chengdu, Nanning, and Zhengzhou, were compared against their multi-temporal Landsat images (Fig. 7). Generally, our results provide accurate representation of urban land and reliable monitoring of urban dynamics. Based on the mapping results, urban expansion in the urban fringe of Shanghai is the most active, especially in the southeast area. In Chengdu, the urban land was expanding to the north and southwest. In the case of Nanning, the urban land expanded mainly on the fringes, and meanwhile, new urban areas appeared in the southwest of the city. Zhengzhou's urban land was sprawling towards the east.

To further assess the reliability of the MGUP products, they were compared to MCD12Q1.v5, MCD12Q1.v6, and CCI-LC through visual inspection. The urban dynamics for the 4 representative cities, Berlin (Germany), Chicago (United States), Cape Town (South Africa), and Shanghai (China), are presented in Fig. 8. In addition, the zoom-in results corresponding to the yellow frames in Fig. 8 are shown in Fig. 9. It can be seen that by referring to the Landsat and Google images, MGUP and CCI-LC can delineate urban areas more accurately with fine spatial details. However, the two MCD12Q1 products show slight over-estimation in the urban core and under-estimation in the outskirts (See Fig. R1). With respect to temporal dynamics of urban areas, the MGUP products present better quality in both spatial and temporal distribution. Please notice that MGUP and MCD12Q1 products are based on the MODIS images, but better results are observed for the former, since MGUP strengthened the number and quality of the training samples by effectively integrating the existing state-of-the-art global datasets.

3.2. Quantitative accuracy assessment

F-score values for the four global products at global scale are compared in Fig. 10. Our results have the greatest F-scores in most years. Only in 2010, the F-score of our results is slightly smaller than the one of CCI-LC by 0.004. There is variability in accuracies among different years since the validation cities chosen for each year are different. For instance, the number of the relatively small-size cities selected for validation in 2016 is more than that in other years, therefore, their accurate mapping is challenging and relatively lower accuracy is obtained (Schneider et al., 2010).

Furthermore, Fig. 11(a) and (b) show the mapping accuracies at different cities and continents, respectively. MGUP acquires the highest accuracy in all the city levels. The F-score of MGUP for all the validation cities is 0.88, followed by CCI-LC (0.86), MCD12Q1.v6 (0.86), and MCD12Q1.v5 (0.82). The F-scores of our results for the first-, second- and third-level cities are 0.9079, 0.8521, and 0.7512, respectively, reflecting a tendency that the accuracy decreases with low city levels (corresponding to small-size urban areas). This phenomenon also occurs in the other global products, and a possible reason is the lack of representative urban features and fragmented urban morphology in the low level cities. However, our results are still better than other products in the thrid-level cities, and outperform the second best CCI-LC by an increase of 0.037 in F-score. The improved accuracy of MGUP in the third-level cities can be explained by the following two factors: (1) The proposed sample extraction method can generate diverse and representative samples; and (2) The locally-adaptive classification can take into account the regional differences in urban morphology.

As for the continent-level accuracy evaluation, MGUP achieves the highest F-score in North America, South America, Asia, and Europe; and the F-score of MGUP is slightly smaller by 0.006 in Africa than that of MCD12Q1.v6 and 0.008 in Oceania than that of CCI-LC, respectively.

Table 4
The detailed information including countries and continents of the 135 validation cities.

2002		2004	2006		2008	2010								
City	Country	Continent	City	Country	Continent	City	Country	Continent	City	Country	Continent	City	Country	Continent
1 Karachi	Pakistan	Asia	1 Istanbul	Turkey	Asia	1 Bangkok	Thailand	Asia	1 Shenzhen	China	Asia	1 Karachi	Pakistan	Asia
2 Barcelona	Spain	Europe	2 Chongqing	China	Asia	2 Barcelona	Spain	Europe	2 Mexico City	Mexico	North America	2 Jakarta	Indonesia	Asia
3 Shanghai	China	Asia	3 Los Angeles	America	North America	3 Buenos Aires	Argentina	South America	3 Sao Paulo	Brazil	South America	3 Osaka	Japan	Asia
4 Istanbul	Turkey	Asia	4 Sao Paulo	Brazil	South America	4 Beijing	China	Asia	4 Paris	France	Europe	4 Mexico City	Mexico	North America
5 Cairo	Egypt	Africa	5 Paris	France	Europe	5 Moscow	Russia	Europe	5 Man Nila	Philippines	Asia	5 Sao Paulo	Brazil	South America
6 Umm Durman	Sudan	Africa	6 Hanoi	Vietnam	Asia	6 Guarulhos	Brazil	South America	6 Lusaka	Zambia	Africa	6 Ho Chi Minh	Vietnam	Asia
7 Baltimore	America	North America	7 Sydney	Australia	Oceania	7 Changsha	China	Asia	7 Montreal	Canada	North America	7 Addis Ababa	Ethiopia	Africa
8 Naples	Italy	Europe	8 Minneapolis	America	North America	8 Vienna	Austria	Europe	8 Santa Cruz	Bolivia	South America	8 Warsaw	Poland	Europe
9 Zhaoqing	China	Asia	9 Baghdad	Iraq	Asia	9 Monterrey	America	North America	9 Ahmedabad	India	Asia	9 Kabul	Afghanistan	Asia
10 Santiago	Chile	South America	10 Belgrade	Serbia	Europe	10 Adelaide	Australia	Oceania	10 Beirut	Lebanon	Asia	10 San Diego	America	North America
11 Qufu	China	Asia	11 Temuco	Chile	South America	11 Sinop	Brazil	South America	11 Uman	Ukraine	Europe	11 Nanning	China	Asia
12 Jequie	Brazil	South America	12 Matsuyama	Japan	Asia	12 Saint Catherine	Canada	North America	12 Cheonan	South Korea	Asia	12 Texacomora	Mexico	North America
13 Salt Lake City	America	North America	13 Batumi	Georgia	Europe	13 Arzars	Russia	Europe	13 Fort Worth	America	North America	13 Madison	America	North America
14 Khomeini	Iran	Asia	14 Murahara	India	Asia	14 Kina	Egypt	Africa	14 Florida Budaca	Columbia	South America	14 Severodvinsk	Russia	Europe
15 Junagadh	India	Asia	15 Ulaanbaatar	Mongolia	Asia	15 Gold Coast	Australia	Oceania	15 Bayamo	Cuba	North America	15 Ain Oussera	Algeria	Africa
2012			2014			2016			2018					
City	Country	Continent	City	Country	Continent	City	Country	Continent	City	Country	Continent			
1 Moscow	Russia	Europe	1 Lahore	Pakistan	Asia	1 Delhi	India	Asia	1 Tianjin	China	Asia			
2 Seoul	South Korea	Asia	2 Man Nila	Philippines	Asia	2 Beijing	China	Asia	2 Istanbul	Turkey	Asia			
3 Los Angeles	America	North America	3 Tokyo	Japan	Asia	3 Lagos	Nigeria	Africa	3 Buenos Aires	Argentina	South America			
4 Buenos Aires	Argentina	Europe	4 Los Angeles	America	North America	4 Lima	Peru	South America	4 Mumbai	India	Asia			
5 Mumbai	India	Asia	5 Sao Paulo	Brazil	South America	5 Jakarta	Indonesia	Asia	5 Bogota	Colombia	South America			
6 Harare	Zimbabwe	Africa	6 Medan	Indonesia	Asia	6 Shiraz	Iran	Asia	6 Singapore	Singapore	Asia			
7 Hefei	China	Asia	7 Bamako	Mali	Africa	7 Pretoria	South Africa	Afirca	7 Kampala	Uganda	Africa			
8 Phoenix	America	North America	8 Calgary	Canada	North America	8 Cincinnati	America	North America	8 Chicago	America	North America			
9 Donetsk	Ukraine	Europe	9 Sapporo	Japan	Asia	9 Tbilisi	Grunia	Asia	9 Suwon	South Korea	Asia			
10 Urumqi	China	Asia	10 Worcester	England	Europe	10 Milan	Italy	Europe	10 Ufa	Russa	Europe			
11 Kot Adu	Pakistan	Asia	11 Jinchang	China	Asia	11 Vancouver	Canada	North America	11 Kansas	America	North America			
12 Winnipeg	Canada	North America	12 Khammouan	Laos	Asia	12 Lhasa	China	Asia	12 Ural	Kazakhstan	Asia			
13 Quetzaltenango	Guatemala	South America	13 Thika	Kenya	Africa	13 Itajai	Brazil	South America	13 Hanzhong	China	Asia			
14 Cuttack	India	Asia	14 Teofilo Otoni	Brazil	South America	14 Tyre	Lebanon	Asia	14 Villaverde	Spain	Europe			
15 Leipzig	Germany	Europe	15 Atlanta	America	North America	15 Kindia	Guinea	Africa	15 Iquitos	Peru	South America			

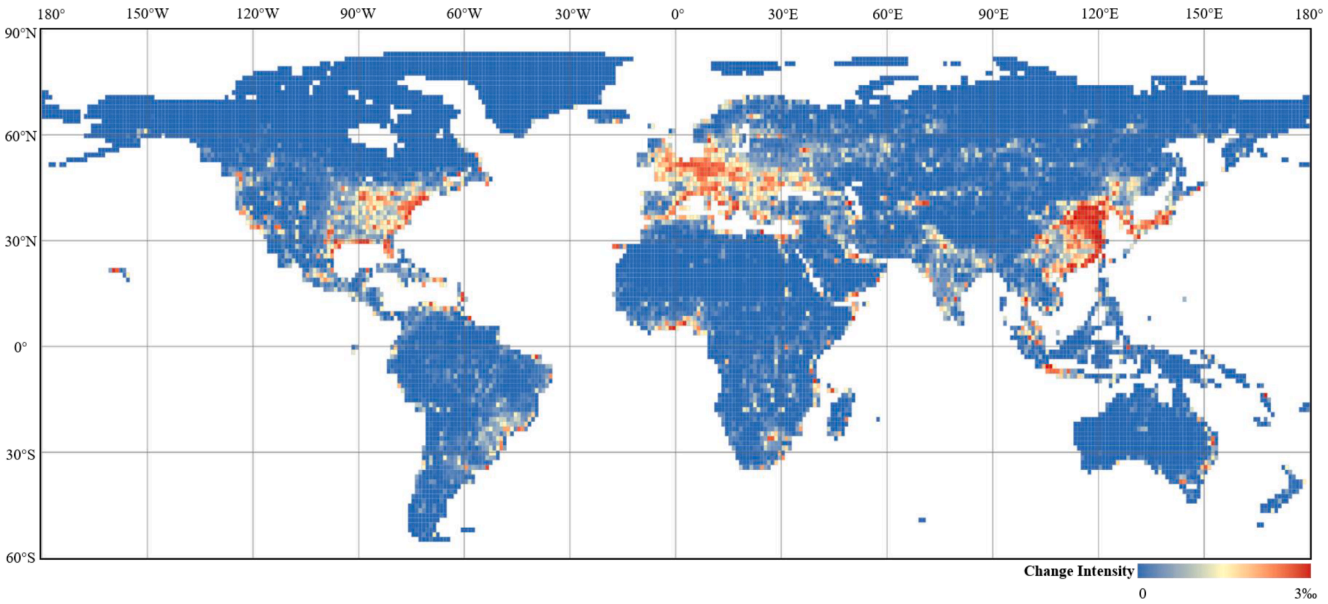

Fig. 5. Global change intensity map at a grid scale of 1° during 2001 ~ 2018.

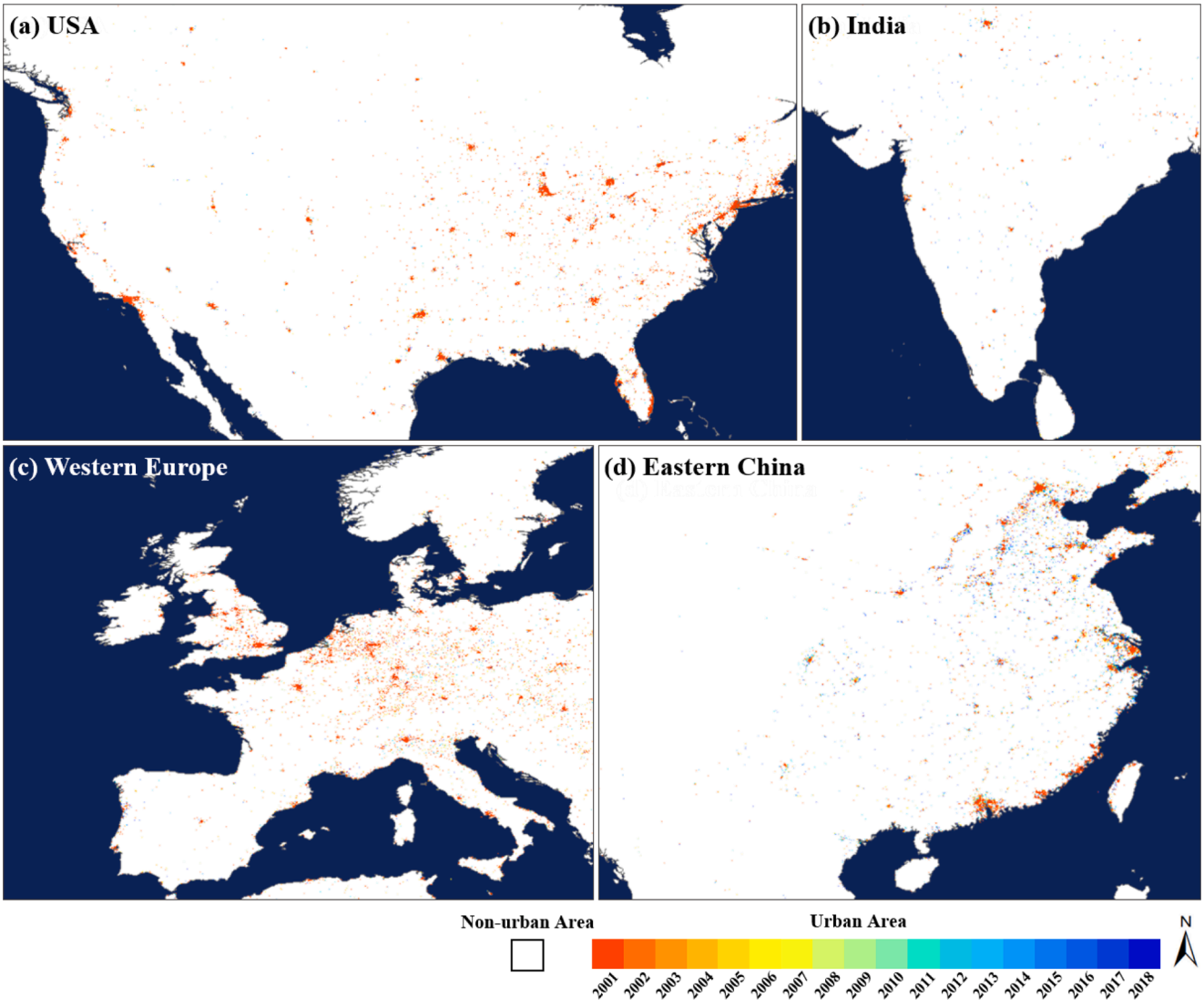

Fig. 6. Mapping results of MGUP for the 4 representative hotspot regions: (a) United States, (b) India, (c) Western Europe, and (d) Eastern China.

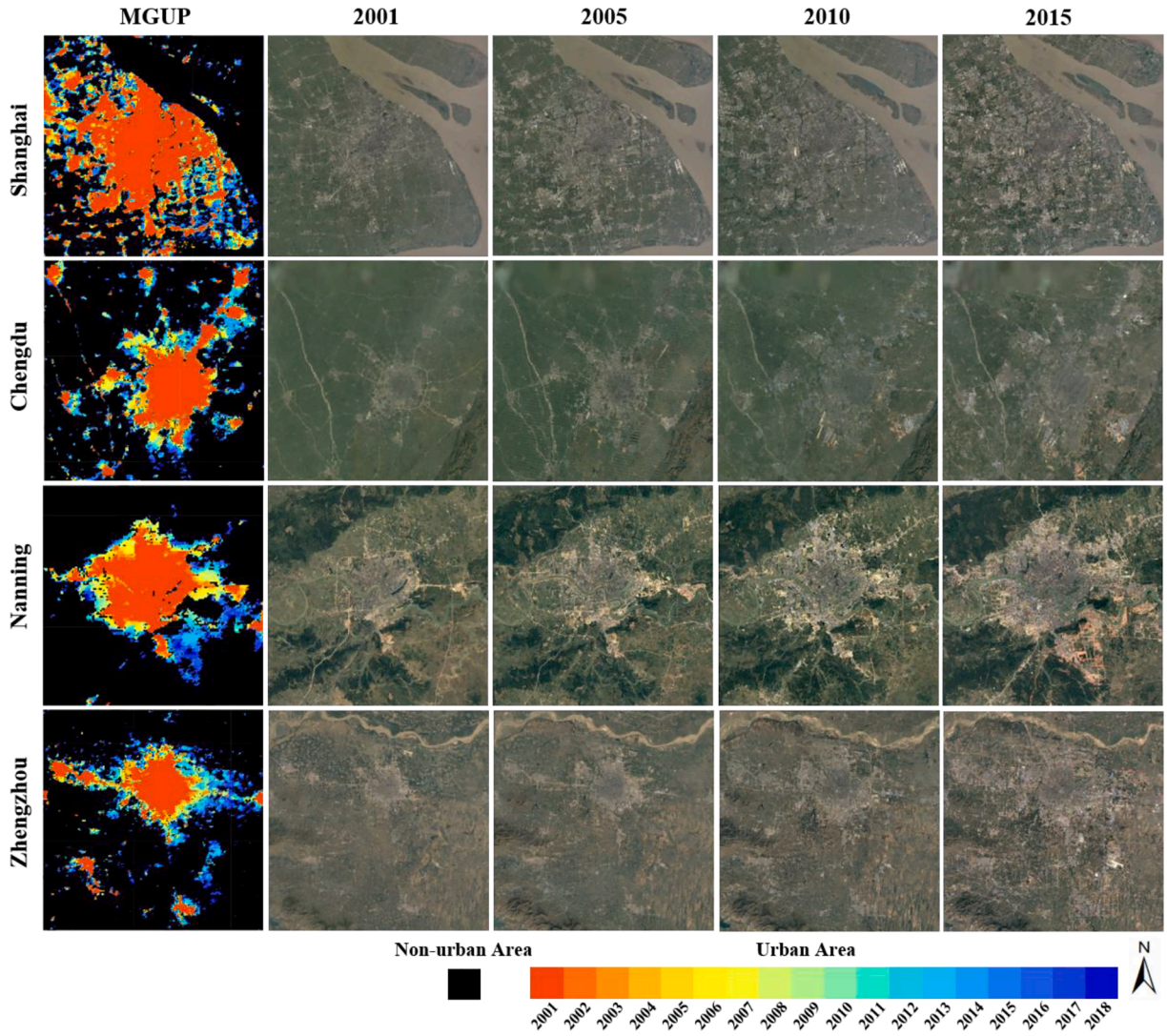

Fig. 7. Mapping results of MGUP for the 4 representative Chinese cities.

The relatively poorer performance in Africa and Oceania can be possibly attributed to the confusion of spectrally similar classes, bare soil and urban land. Specifically, there is great inconsistency among different URB datasets in these two continents, resulting in lack of high-quality samples for the proposed automated sampling strategy. However, this issue can be well addressed by adding more reliable samples to these regions in future work.

To assess the quality of the training samples, two representative countries, i.e., China and USA, has been regarded as the test areas. For China, a 30 m land cover product CLUD (China's Land-Use/cover Datasets) in 2005, 2010, 2015 were used as the reference (Liu et al.,2014), and for USA, the 30 m NLCD (National Land Cover Database) (Fry et al.,2011) in 2006, 2011, 2016 were adopted as the reference. The accuracy of the automatically selected samples is assessed in Table 5. Considering that the RF classifier used in our research is robust to the random noise and is tolerant to the noise level up to 25%–30% (Pelletier et al., 2017), it can be stated that our automatically generated samples are satisfactory.

To investigate the effect of the features, the permutation-based importance of each feature is measured (Breiman, 2001) and shown in Fig. 12. It can be seen that in all the seasons, spectral features and their difference indexes (NDXI) show similar contributions to classification, and the night time LST features are the most important. Among the spectral bands, band2 and band5 are of higher importance. In general, the feature importance in the four seasons shows similar patterns.

3.3. Analysis of urban expansion

Based on the annual MGUP from 2001 to 2018, urban expansion at global, continent, and national scale was analyzed.

3.3.1. Urban expansion at global scale

Fig. 13 shows the annual dynamics of global urban area from 2001 to 2018 for the four global products. As indicated by MGUP and CCI-LC, global urban area is rapidly and continuously increasing, which is consistent to the visual inspection in Section 3.1. A linear and slow growth trend is observed for MCD12Q1.v6, whereas almost no dynamic change is found in MCD12Q1.v5. The global urban areas derived from MGUP exhibit high agreement with those from CCI-LC in most years with a slight difference in 2015–2018. In contrast to MCD12Q1.v5, MGUP shows smaller global urban areas during 2001 ~ 2010 but higher values after 2010. Compared with MCD12Q1.v6, MGUP has less urban area during 2001 ~ 2016, and becomes the same from 2017. It should be emphasized that MGUP, MCD12Q1.v5, and MCD12Q1.v6 are all MODIS-based products and the main data sources for CCI-LC are Medium Resolution Imaging Spectrometer (MERIS) imagery. However,

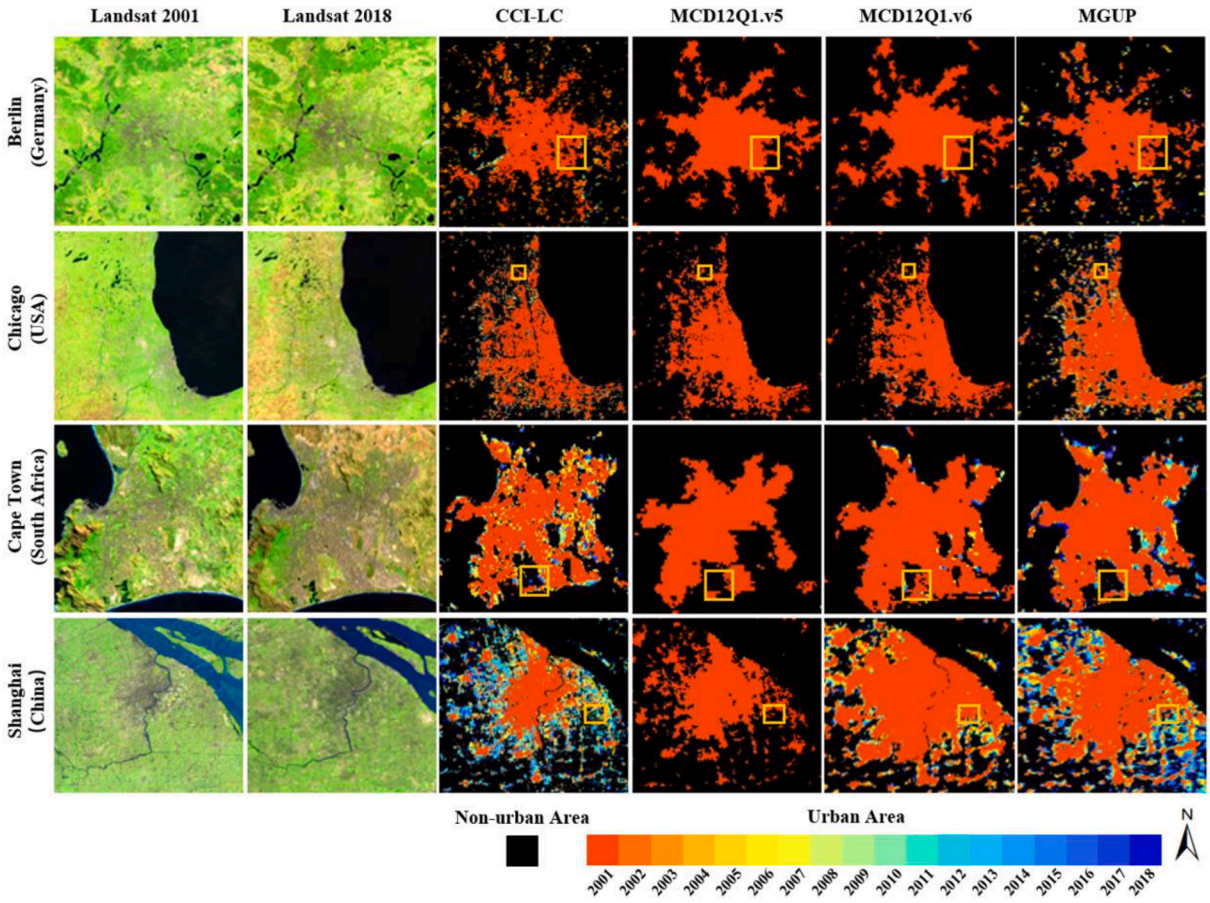

Fig. 8. Comparison of the urban dynamics for the 4 representative cities in MGUP, CCI-LC, MCD12Q1.v5, and MCD12Q1.v6.

although different data sources are used for MGUP and CCI-LC, their annual dynamics of global urban area are highly similar, implying the reliability of both products. In summary, we can conclude that the proposed automatic sample extraction method can effectively collect global time-series urban and non-urban samples and the presented MGUP is an improved version of the existing MODIS-based urban products.

3.3.2. Urban expansion at continent scale

Based on the MGUP, the urban area for each continent is compared in Fig. 14. Urban density, i.e., the percentage of urban area size in the total land area, can partly reflect urbanization level. Urban area (density) in 2018 is 304,575 km^2 (0.68%) in Asia, 201,512 km^2 (0.84%) in North America, 180,549 km^2 (1.78%) in Europe, 52,835 km^2 (0.30%) in South America, 49,772 km^2 (0.17%) in Africa, 12,989 km^2 (0.15%) in Oceania, respectively. Even though the total land area in Asia is the largest and about two times as large as that in Europe, its urban density is still lower than Europe and North America. Only the urban density for Europe, North America, and Asia is larger than the global average (0.54%) with that of Europe (1.78%) significantly higher than that of other continents.

Regarding the annual dynamic, there is a rapid increase of urban area in Asia, South America, and Africa, whereas a steady increase trend is observed for North America, Europe, and Oceania. The largest increase in urban area occurs in Asia from 2001 to 2018 (156,344 km^2), followed by Europe (65,886 km^2), North America (55,839 km^2), Africa (27,685 km^2), South America (18,134 km^2), and Oceania (3245 km^2). As for the percentage of the urban area for each continent in the global total urban area, it has increased from 31% in 2001 to 38% in 2018 for Asia. However, a decreased trend is observed for Europe (from 24% in 2001 to 22% in 2018) and North America (from 30% in 2001 to 25% in 2018). The percentages for Africa, South America, and Oceania vary little during the period, and the variations are no more than 1%.

3.3.3. Urban expansion at national scale

The area and rate of urban growth at national scale from 2001 to 2018 are shown in Fig. 15(a) and (b), respectively. The urban expansion at national scale is found to be unevenly distributed, and is intensive mainly in North America, Asia, and South America. The top four countries having the largest urban area increment are China (92,645 km^2), United States (43,594 km^2), Russia (13,405 km^2), and India (11,294 km^2). The increment of China accounts for 28% of total urban area change in Asia, and is 3.6 times the sum of the increase in Russia and India. The urban expansion in Europe and North America (except for Greenland) is spatially even. Urban expansion in South America is mainly concentrated in the eastern Brazil and southern Argentina, and the rest of South America experiences relatively small urban sprawl. In Africa, most countries have smaller urban area change except for South Africa (4020 km^2) and Nigeria (4145 km^2).

In contrast, the spatial distribution of the urban growth rate is quite different from that of the growth area at the national level. The countries having high growth rates mainly involve developing countries in Africa and Asia. The growth rates in most Africa countries are high, which exceed 200% in Africa West and South. As for Asia, countries with high growth rates are mainly located in East, South, and Southeast Asia. It is worthy noticing that both urban growth area and rate are high in Asia.

4. Conclusions

In this research, we proposed an automated global sample extraction scheme, and produced 250-m urban extent datasets from 2001 to 2018

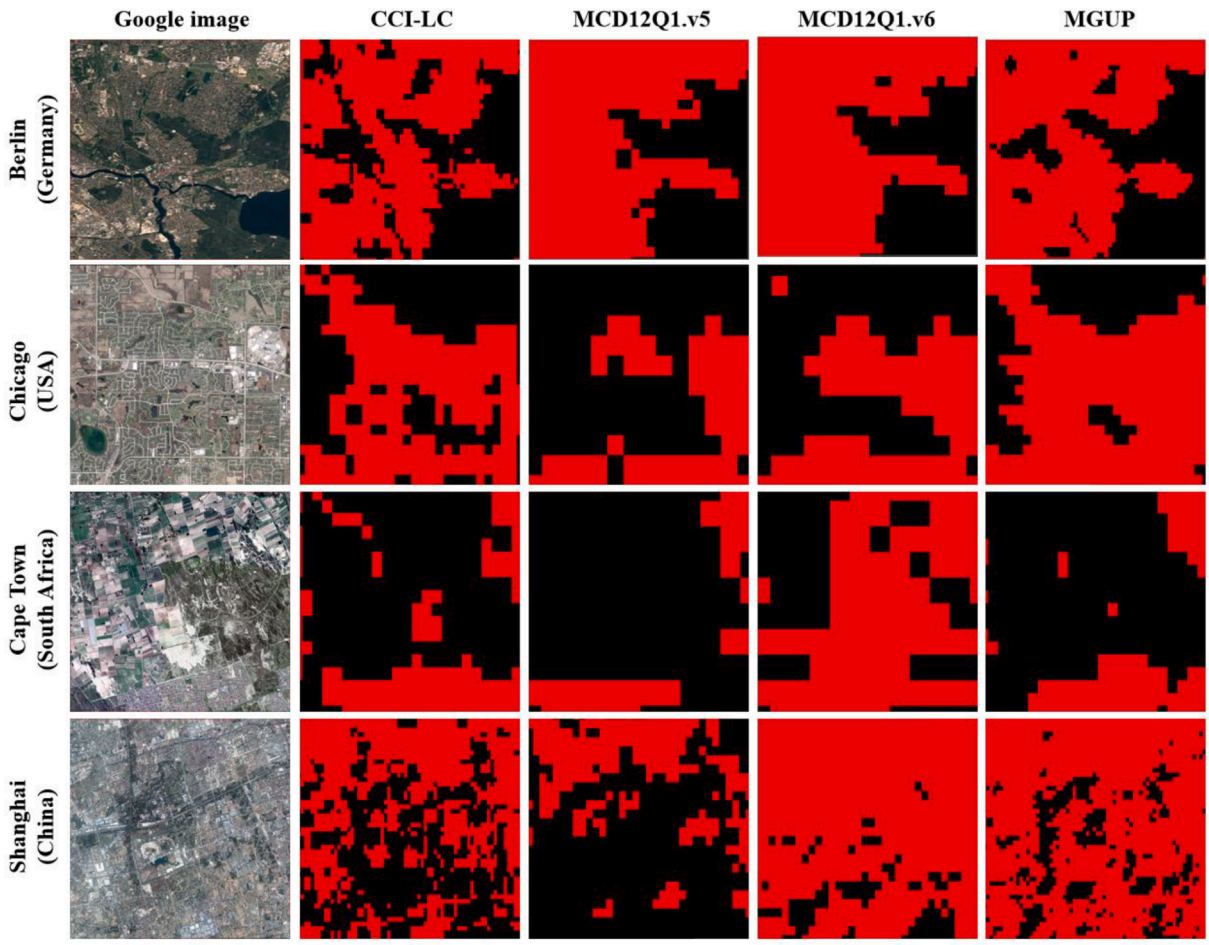

Fig. 9. The zoom-in results of MGUP, CCI-LC, MCD12Q1.v5, and MCD12Q1.v6, corresponding to the yellow frames in Fig. 8, used to highlight the over-estimation in the urban core and the under-estimation in the outskirts. (For interpretation of the references to colour in this figure legend, the reader is referred to the web version of this article.)

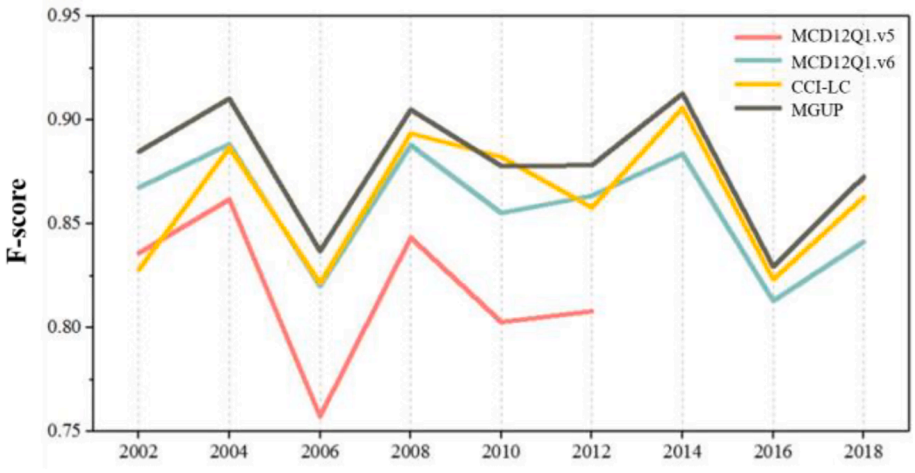

Fig. 10. F-score values at global scale for different years.

using MODIS imagery. Using our validation samples, the global level F-score for this dataset is as high as 0.88, achieving better results than the current state-of-the-art global products with similar spatial resolution, i.e., MCD12Q1.v5 (0.82), MCD12Q1.v6 (0.86), and CCI-LC (0.86). MGUP achieves the most accurate results in different years, different level cities, and different continents. The results reveal that the proposed method can effectively collect global time-series urban and non-urban samples and the MGUP can be regarded as an improved version of the existing MODIS-based urban products (e.g., MCD12Q1.v5 and MCD12Q1.v6) and a reliable data source for monitoring the global urban expansion. It should be acknowledged that the relatively higher accuracy of MGUP is attributed to the fusion of the current state-of-the-

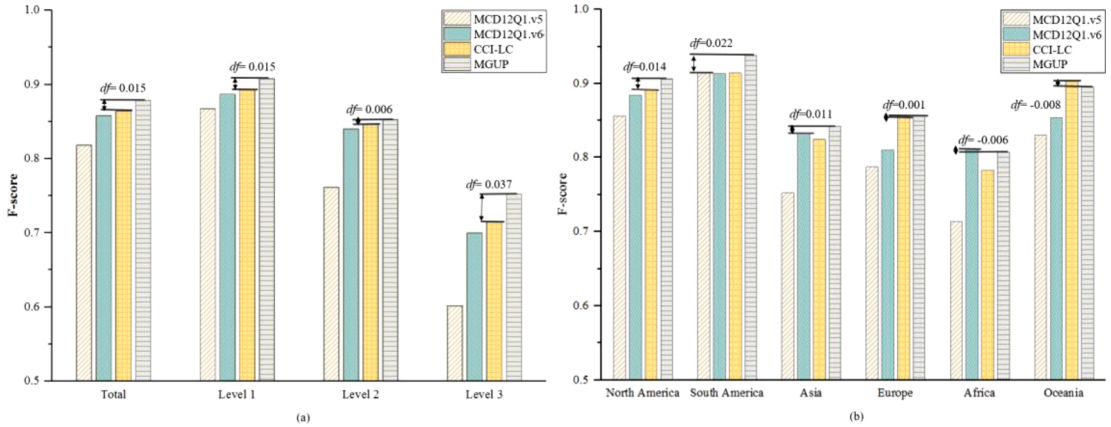

Fig. 11. F-score values at different (a) level cities and (b) continents.

Table 5
Accuracy of the automatically selected samples.

Test Area	Year	Urban Samples	Nonurban Samples
China	2005	0.8214	0.9834
	2010	0.8882	0.9808
	2015	0.8470	0.9757
USA	2006	0.7884	0.9991
	2011	0.7840	0.9990
	2016	0.8137	0.9988

art products as well as the proposed mapping strategy, e.g., sample refinement, locally adaptive classifier, and the spatio-temporal post-processing.

In terms of MGUP, the world's urban land area increased to 802,233 km^2, accounting for 0.54% of the Earth's land surface in 2018. In continent level, urban area (density) in 2018 was 304,575 km^2 (0.68%) in Asia, 201,512 km^2 (0.84%) in North America, 180,549 km^2 (1.78%) in Europe, 52,835 km^2 (0.30%) in South America, 49,772 km^2 (0.17%) in Africa, 12,989 km^2 (0.15%) in Oceania, respectively. There was a rapid increase of urban area in Asia, South America, and Africa, whereas relatively steady increase trend is observed for North America, Europe, and Oceania. In national level, urban area increments are high mainly in North America, Asia, and South America; and countries having high growth rates mainly involve developing countries in Africa and Asia. The top four countries having the largest urban area increment are China (92,645 km^2), United States (43,594 km^2), Russia (13,405 km^2), and India (11,294 km^2).

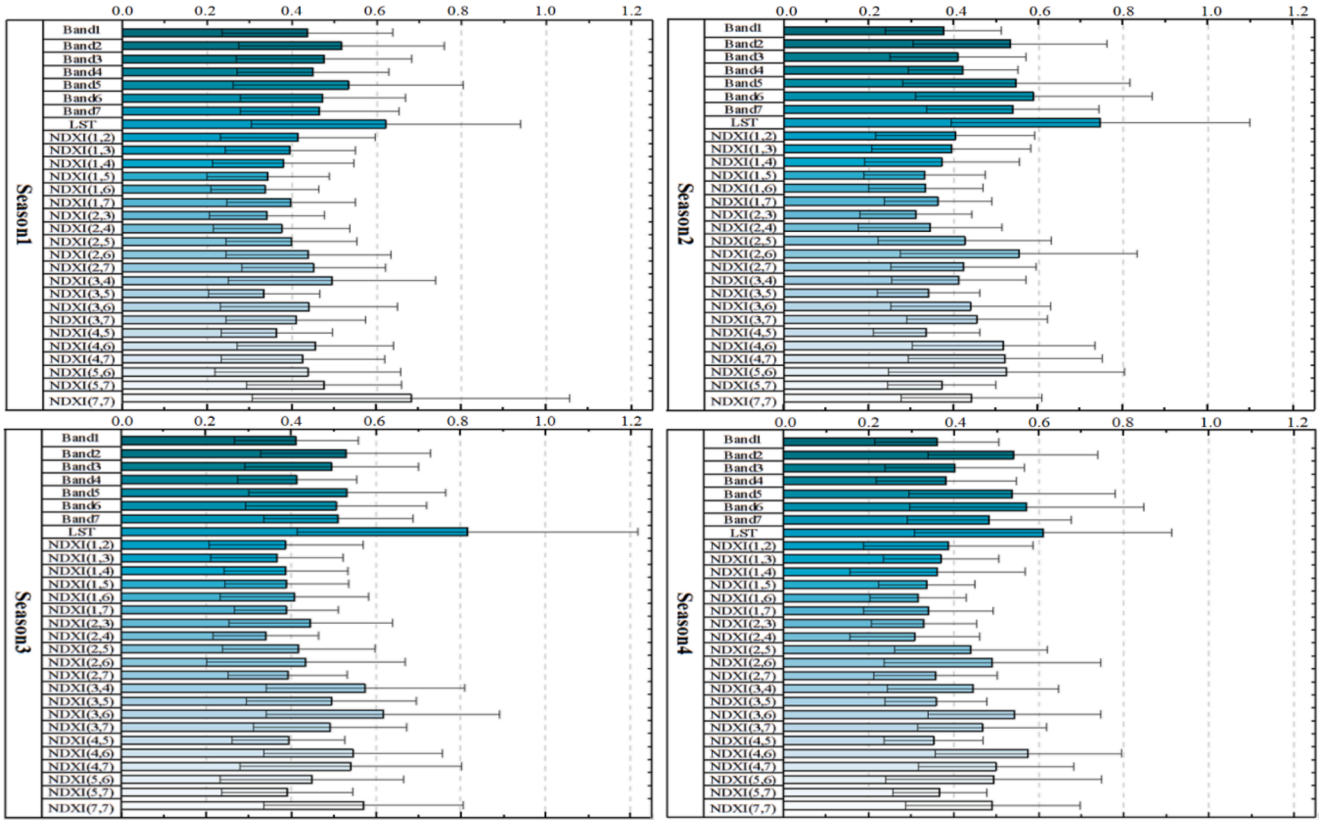

Fig. 12. Feature importance in the four seasons. The bar indicates the average feature importance calculated in different grids, and the error bar denotes their standard deviation.

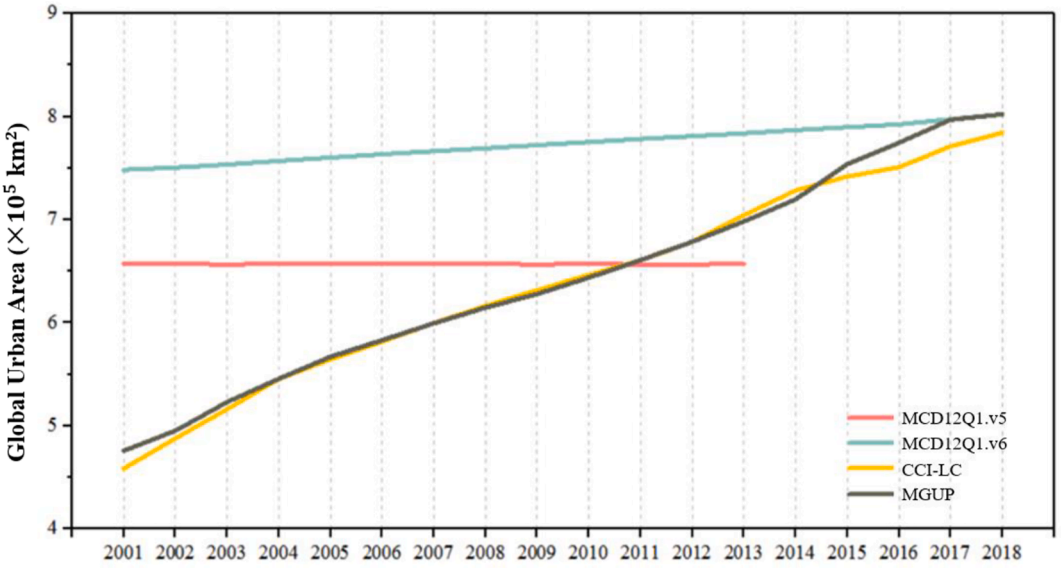

Fig. 13. Annual dynamics of global urban area from 2001 to 2018.

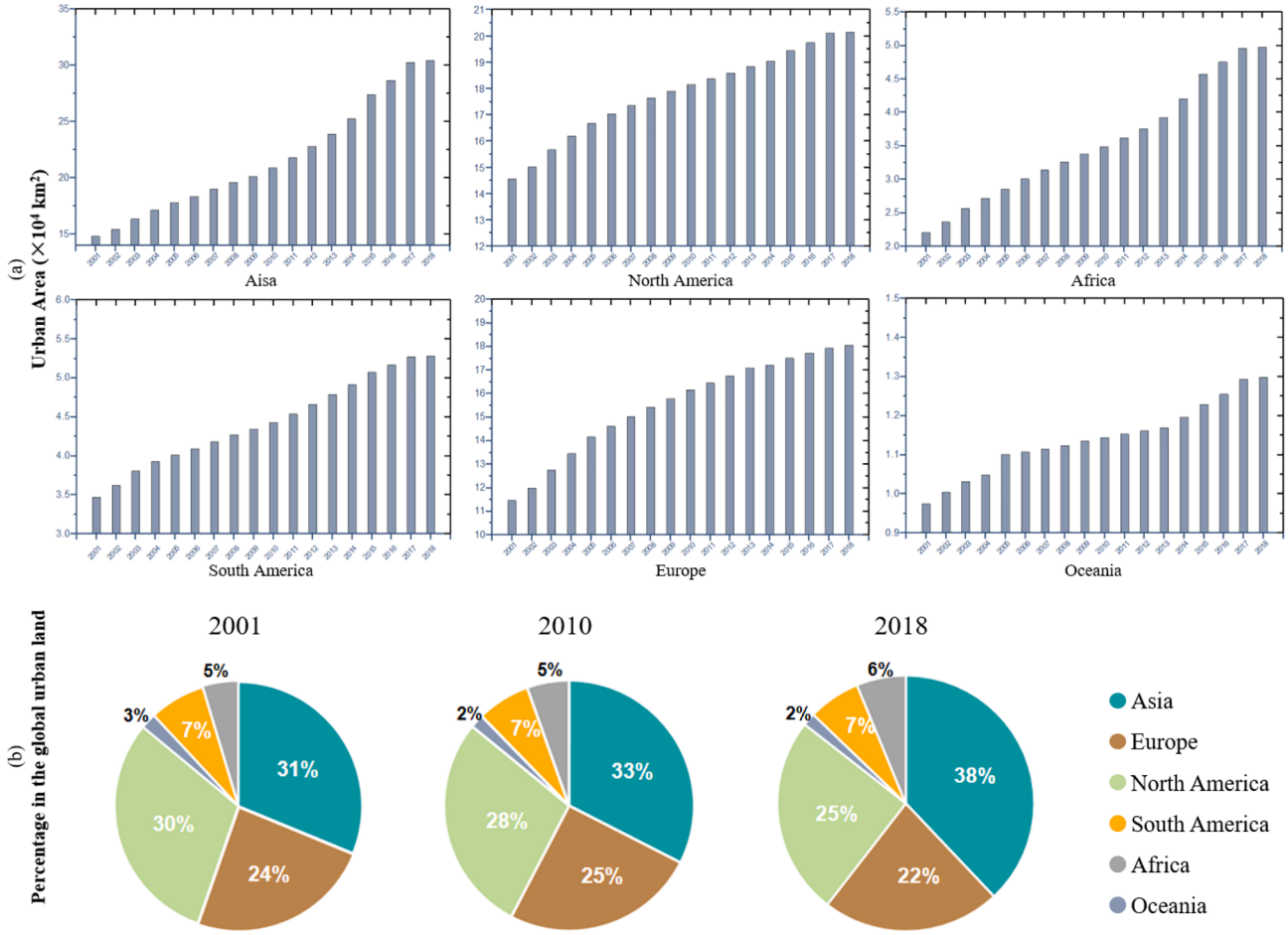

Fig. 14. Annual dynamics of urban area in different continents from 2001 to 2018: (a) urban area and (b) their percentage in the global urban land.

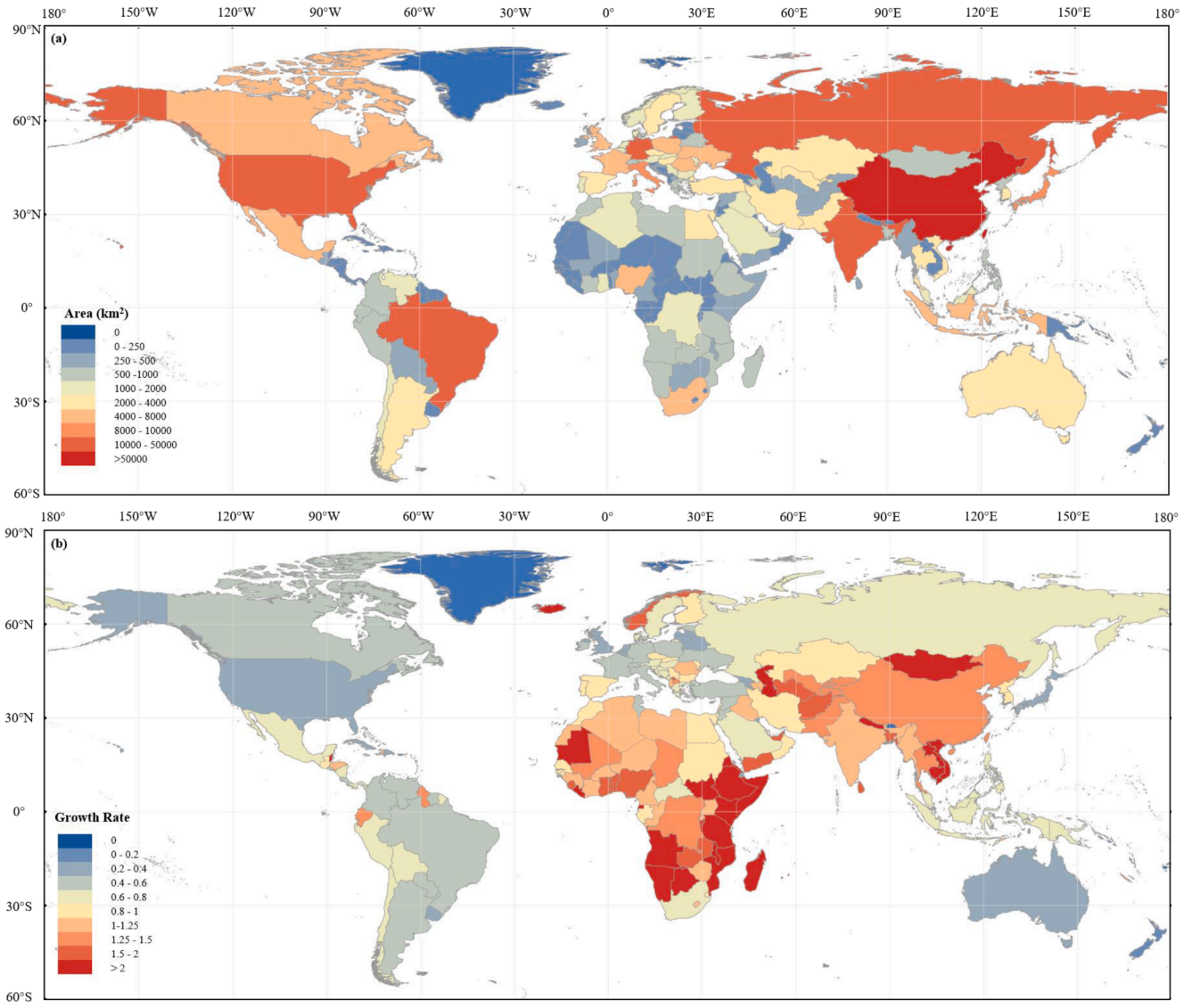

Fig. 15. Urban expansion at national scale from 2001 to 2018: (a) growth area and (b) growth rate.

Declaration of Competing Interest

The authors declare that they have no known competing financial interests or personal relationships that could have appeared to influence the work reported in this paper.

Acknowledgement

The research was supported by the National Natural Science Foundation of China under Grants 41701382, 41771360 and 41971295, the National Program for Support of Top-notch Young Professionals, the Hubei Provincial Natural Science Foundation of China under Grant 2017CFA029, and the National Key R&D Program of China under Grant 2016YFB0501403.

References

Bartholome, E., Belward, A.S., 2005. GLC2000: a new approach to global land cover mapping from Earth observation data. Int. J. Remote Sens. 26, 1959–1977.
Bontemps, S., Defourny, P., Van Bogaert, E., Arino, O., Kalogirou, V., Perez, J.R., 2011. GLOBCOVER 2009-Products description and validation report. Retrieved from http://due.esrin.esa.int/files/p68/GLOBCOVER2009_Validation_Report_2.2.pdf.
Boschetti, L., Roy, D.P., Justice, C.O., Humber, M.L., 2015. MODIS–Landsat fusion for large area 30 m burned area mapping. Remote Sens. Environ. 161, 27–42.
Breiman, L., 2001. Random forests. Mach. Learn. 45, 5–32.
Carlson, T.N., Arthur, S.T., 2000. The impact of land use—land cover changes due to urbanization on surface microclimate and hydrology: a satellite perspective. Global Planet. Change 25, 49–65.
Chen, J., Chen, J., Liao, A., Cao, X., Chen, L., Chen, X., He, C., Han, G., Peng, S., Lu, M., Zhang, W., Tong, X., Mills, J., 2015. Global land cover mapping at 30m resolution: A POK-based operational approach. ISPRS J. Photogramm. Remote Sens. 103, 7–27.
Chen, Z., Yu, B., Zhou, Y., Liu, H., Yang, C., Shi, K., Wu, J., 2019. Mapping global Urban areas from 2000 to 2012 using time-series nighttime light data and MODIS products. IEEE J. Sel. Top. Appl. Earth Obs. Remote Sens. 12, 1143–1153.
CIESIN, 2004. Global Rural-Urban Mapping Project (GRUMP). Urban Extents Grids. Database, Alpha Version.
Defourny, P., Vancutsem, C., Bicheron, P., Brockmann, C., Nino, F., Schouten, L., Leroy, M., 2006. GLOBCOVER: a 300 m global land cover product for 2005 using Envisat MERIS time series. Proceedings of the ISPRS commission VII mid-term symposium: remote sensing: from pixels to processes, 538–542.
ESA, 2017. Land cover CCI product user guide version 2. Retrieved from http://maps.elie.ucl.ac.be/CCI/viewer/download/ESACCI-LC-Ph2-PUGv2_2.0.pdf.
Estel, S., Kuemmerle, T., Alcántara, C., Levers, C., Prishchepov, A., Hostert, P., 2015. Mapping farmland abandonment and recultivation across Europe using MODIS NDVI time series. Remote Sens. Environ. 163, 312–325.
Friedl, M.A., Sulla-Menashe, D., Tan, B., Schneider, A., Ramankutty, N., Sibley, A., Huang, X., 2010. MODIS Collection 5 global land cover: Algorithm refinements and characterization of new datasets. Remote Sens. Environ. 114, 168–182.
Fry, J.A., Xian, G., Jin, S., Dewitz, J.A., Homer, C.G., Yang, L., Barnes, C.A., Herold, N.D., Wickham, J.D., 2011. Completion of the 2006 National Land Cover Database for the conterminous United States. Photogramm. Eng. Remote Sens. 77, 858–864.
Gislason, P.O., Benediktsson, J.A., Sveinsson, J.R., 2006. Random forests for land cover classification. Pattern Recogn. Lett. 27, 294–300.

Gong, P., Li, X., Wang, J., Bai, Y., Chen, B., Hu, T., Liu, X., Xu, B., Yang, J., Zhang, W., Zhou, Y., 2020. Annual maps of global artificial impervious area (GAIA) between 1985 and 2018. Remote Sens. Environ. 236, 111510.
Gong, P., Wang, J., Yu, L., Zhao, Y., Zhao, Y., Liang, L., Niu, Z., Huang, X., Fu, H., Liu, S., 2013. Finer resolution observation and monitoring of global land cover: First mapping results with Landsat TM and ETM+ data. Int. J. Remote Sens. 34, 2607–2654.
Han, L., Zhou, W., Li, W., Li, L., 2014. Impact of urbanization level on urban air quality: A case of fine particles (PM2. 5) in Chinese cities. Environ. Pollut. 194, 163–170.
Heydari, S.S., Mountrakis, G., 2018. Effect of classifier selection, reference sample size, reference class distribution and scene heterogeneity in per-pixel classification accuracy using 26 Landsat sites. Remote Sens. Environ. 204, 648–658.
Huang, X., Schneider, A., Friedl, M.A., 2016. Mapping sub-pixel urban expansion in China using MODIS and DMSP/OLS nighttime lights. Remote Sens. Environ. 175, 92–108.
Keramitsoglou, I., Kiranoudis, C.T., Ceriola, G., Weng, Q., Rajasekar, U., 2011. Identification and analysis of urban surface temperature patterns in Greater Athens, Greece, using MODIS imagery. Remote Sens. Environ. 115, 3080–3090.
Kullback, S., Leibler, R.A., 1951. On information and sufficiency. Ann. Math. Stat. 22, 79–86.
Latham, J., Cumani, R., Rosati, I., Bloise, M., 2014. Global land cover share (GLC-SHARE) database beta-release version 1.0-2014. Retrieved from http://www.fao.org/uploads/media/glc-share-doc.pdf.
Li, C., Wang, J., Wang, L., Hu, L., Gong, P., 2014. Comparison of classification algorithms and training sample sizes in urban land classification with Landsat thematic mapper imagery. Remote Sensing 6, 964–983.
Li, J., Huang, X., Hu, T., Jia, X., Benediktsson, J.A., 2019. A novel unsupervised sample collection method for urban land-cover mapping using landsat imagery. IEEE Trans. Geosci. Remote Sens. 57, 3933–3951.
Li, Y., Li, Y., Zhou, Y., Shi, Y., Zhu, X., 2012. Investigation of a coupling model of coordination between urbanization and the environment. J. Environ. Manage. 98, 127–133.
Liu, J., Kuang, W., Zhang, Z., Xu, X., Qin, Y., Ning, J., Zhou, W., Zhang, S., Li, R., Yan, C., Wu, S., Shi, X., Jiang, N., Yu, D., Pan, X., Chi, W., 2014. Spatiotemporal characteristics, patterns, and causes of land-use changes in China since the late 1980s. J. Geog. Sci. 24, 195–210.
Liu, S., Su, H., Cao, G., Wang, S., Guan, Q., 2019. Learning from data: A post classification method for annual land cover analysis in urban areas. ISPRS J. Photogramm. Remote Sens. 154, 202–215.
Liu, X., Hu, G., Chen, Y., Li, X., Xu, X., Li, S., Pei, F., Wang, S., 2018. High-resolution multi-temporal mapping of global urban land using Landsat images based on the Google Earth Engine Platform. Remote Sens. Environ. 209, 227–239.
Madlener, R., Sunak, Y., 2011. Impacts of urbanization on urban structures and energy demand: What can we learn for urban energy planning and urbanization management? Sustain. Cities Soc. 1, 45–53.
McDonald, R.I., Marcotullio, P.J., Güneralp, B., 2013. Urbanization and global trends in biodiversity and ecosystem services. Urbanization, biodiversity and ecosystem services: Challenges and opportunities. Retrieved from https://link.springer.com/book/10.1007/978-94-007-7088-1.
Mertes, C.M., Schneider, A., Sulla-Menashe, D., Tatem, A., Tan, B., 2015. Detecting change in urban areas at continental scales with MODIS data. Remote Sens. Environ. 158, 331–347.
Moore, M., Gould, P., Keary, B.S., 2003. Global urbanization and impact on health. Int. J. Hyg. Environ. Health 206, 269–278.
Nations, U, 2018. World Urbanization Prospects: The 2018 Revision. Population Division, Department of Economic and Social Affairs. United Nations Publications.
Nicolaou, N., Siddique, N., Custovic, A., 2005. Allergic disease in urban and rural populations: increasing prevalence with increasing urbanization. Allergy 60, 1357–1360.
Pal, M., Mather, P.M., 2006. Some issues in the classification of DAIS hyperspectral data. Int. J. Remote Sens. 27, 2895–2916.
Pauchard, A., Aguayo, M., Peña, E., Urrutia, R., 2006. Multiple effects of urbanization on the biodiversity of developing countries: the case of a fast-growing metropolitan area (Concepción, Chile). Biol. Conserv. 127, 272–281.
Pelletier, C., Valero, S., Inglada, J., Champion, N., Marais Sicre, C., Dedieu, G., 2017. Effect of training class label noise on classification performances for land cover mapping with satellite image time series. Remote Sens. 9, 173.
Poumanyvong, P., Kaneko, S., 2010. Does urbanization lead to less energy use and lower CO2 emissions? A cross-country analysis. Ecol. Econ. 70, 434–444.
Radoux, J., Lamarche, C., Van Bogaert, E., Bontemps, S., Brockmann, C., Defourny, P., 2014. Automated training sample extraction for global land cover mapping. Remote Sens. 6, 3965–3987.
Schneider, A., Friedl, M.A., Potere, D., 2010. Mapping global urban areas using MODIS 500-m data: New methods and datasets based on 'urban ecoregions'. Remote Sens. Environ. 114, 1733–1746.
Schneider, A., Mertes, C., 2014. Expansion and growth in Chinese cities, 1978–2010. Environ. Res. Lett. 9, 024008.
Seto, K.C., Sánchez-Rodríguez, R., Fragkias, M., 2010. The new geography of contemporary urbanization and the environment. Annu. Rev. Environ. Resour. 35, 167–194.
Shao, Z., Fu, H., Li, D., Altan, O., Cheng, T., 2019. Remote sensing monitoring of multi-scale watersheds impermeability for urban hydrological evaluation. Remote Sens. Environ. 232, 111338.
Sulla-Menashe, D., Gray, J.M., Abercrombie, S.P., Friedl, M.A., 2019. Hierarchical mapping of annual global land cover 2001 to present: The MODIS Collection 6 Land Cover product. Remote Sens. Environ. 222, 183–194.
Sung, C.Y., Li, M.-H., 2012. Considering plant phenology for improving the accuracy of urban impervious surface mapping in a subtropical climate regions. Int. J. Remote Sens. 33, 261–275.
Wan, B., Guo, Q., Fang, F., Su, Y., Wang, R., 2015. Mapping US Urban Extents from MODIS Data Using One-Class Classification Method. Remote Sens. 7, 10143–10163.
Wang, J., Zhao, Y., Li, C., Yu, L., Liu, D., Gong, P., 2015. Mapping global land cover in 2001 and 2010 with spatial-temporal consistency at 250 m resolution. ISPRS J. Photogramm. Remote Sens. 103, 38–47.
Wang, L., Li, C., Ying, Q., Cheng, X., Wang, X., Li, X., Hu, L., Liang, L., Yu, L., Huang, H., 2012. China's urban expansion from 1990 to 2010 determined with satellite remote sensing. Chin. Sci. Bull. 57, 2802–2812.
Wehmann, A., Liu, D., 2015. A spatial–temporal contextual Markovian kernel method for multi-temporal land cover mapping. ISPRS J. Photogramm. Remote Sens. 107, 77–89.
Yang, Y., Xiao, P., Feng, X., Li, H., 2017. Accuracy assessment of seven global land cover datasets over China. ISPRS J. Photogramm. Remote Sens. 125, 156–173.
Yifang, B., Gong, P., Gini, C., 2015. Global land cover mapping using Earth observation satellite data: Recent progresses and challenges. ISPRS J. Photogramm. Remote Sens. (Print) 103, 1–6.